Vortex-in-nanodot potentials in thin circular magnetic dots

G. M. Wysin*
Department of Physics, Kansas State University, Manhattan, KS 66506-2601

(Dated: July 8, 2010)

Vortex states in thin circular magnetic nanodots are studied using auxiliary constraining fields as a way to map out the potential energy space of a vortex, while avoiding a rigid vortex approximation. In the model, isotropic Heisenberg exchange competes with the demagnetization field caused both by surface and volume magnetization charge density. The system energy is minimized while applying a constraint on the vortex core position, using Lagrange's method of undetermined multipliers. The undetermined multiplier is seen to be the external field needed to hold the vortex core in place at a desired radial distance r from the dot center. This auxiliary field is applied only in the core region of the vortex. For a uniform nanodot, the potential energy is found to be very close to parabolic with r, as in the rigid vortex approximation, while the constraining field increases linearly with r. Effects of nonmagnetic impurities and holes in the medium can also be estimated. An impurity or hole in the dot can lead to bistable operation between the two minima that result under the application of a transverse applied magnetic field.

PACS numbers: 75.75.+a, 85.70.Ay, 75.10.Hk, 75.40.Mg
Keywords: magnetic vortex, magnetic dot, defects, effective potential

I. INTRODUCTION: MAGNETIC VORTICES IN NANODOTS

Cylindrical magnetic dots of 1–2 μm diameter and thickness 15–100 nm are of great theoretical and experimental interest, because they could serve as high-density memory devices,[1] using a range of materials including Permalloy,[2,3] Fe[4,5] and Co.[6,7] If a dot is very thin compared to its diameter, demagnetization or dipolar effects lead to a nearly planar magnetization (effective easy-plane anisotropy),[8] that depends on position.[9] This leads to vortex states with a curling of the magnetization within the plane of the dot[10,11] and tilting out-of-plane in a vortex core. The core tilting has been used to identify and locate vortices,[12] which have also been identified using magnetic force microscopy.[13] The goal of the present work is to make accurate calculations of the effective space-dependent potential experienced by a vortex within a dot, which will be important for understanding vortex stability, dynamics and manipulation. We consider pure samples as well as those with defined defects or impurities that can pin vortices.[12] The potential due to impurities can be estimated[14,15] from analytic approximations, whereas, here we apply a micromagnetics energy minimization with a constraint on vortex position.

The core spin tilting is similar to that for vortices in easy-plane magnets,[16–18] whose core spins only tilt out of plane when the anisotropy is weaker than a critical strength,[18,19] which originates from an energetic instability.[20–22] The gross effects of defects in magnetic dots, including dipolar effects, can be gleaned from their effects in 2D easy-plane magnets, including only the effects of anisotropic exchange interactions. For instance, in easy-plane magnets (with exchange interactions but no dipolar interactions), theory[23–26] and experiments[27,28] show that nonmagnetic defects attract and pin vortices. Vortex energies are lower on defects[29,30] and defect sites have a thermodynamic preference for vortex formation around their centers.[31] For a vortex pinned on a minimum defect (i.e., one nonmagnetic site in the lattice), all spins obtain a greater tendency to stay close to planar,[29,32] requiring even weaker anisotropy for the core spins to tilt out-of-plane. Considering a hole in the dot as a larger nonmagnetic defect, removing a greater number of magnetic sites beyond some fairly small radius eventually leaves only the planar vortex configuration as the stable one.[33] Dipolar forces strengthen the effective easy-plane anisotropy and enhance the above effects.

When a vortex forms around a defect, some exchange interactions are removed, compared to a vortex far from a defect, leading to a lowered total energy. Pinned vortices in nanoparticles should affect the hysteresis curves[34] and can be manipulated by applied magnetic fields.[12,35] Thus it makes sense to study the potential energy space of vortices in dots with impurities as well as in pure samples. Also of great interest is to consider dots with two or more intentionally designed defects.[36] The vortex can be attracted by any of them, leading to a multistable switching device. For a vortex pinned on a defect, there is a threshold applied field needed to free the vortex from the pinning center.[37] We consider energetics of these states, and how an externally applied magnetic field is able to move a vortex reversibly from a defect and back.

For thin enough dots, there is only weak dependence of magnetization on the (z) coordinate through the thickness. This allows for an approximate two-dimensional analysis that we use here; the three dimensional magnetics is represented quite accurately by a two-dimensional approach.[38,39] Using Green functions for thin samples[40] to obtain the demagnetization field, fast Fourier transforms (FFT) are used for evaluation of the required Green function integrals in only two dimensions. The FFT for finding the demagnetization field[41] in nanomagnetism greatly speeds up this task, which is the calculational bottleneck.

Even in a small dot of 100 nm diameter and 15 nm thickness, there are too many atomic spins to be followed computationally. Instead, the system is partitioned into larger cells containing many atoms; this is the so-called micromagnetics approach.[42] The usual micromagnetics approach uses the Landau-Lifshitz-Gilbert equation with damping to approach a local minimum energy state. Here, we want to impose a desired location to a vortex, and then calculate its energy. The enforcement of this constraint can be accomplished via Lagrange's method of undetermined multipliers, which simultaneously gives the magnitude of the constraining field. We describe how this leads to a new iterative local field relaxation scheme, that is an improvement over earlier approaches.[43]

The result is that the vortex effective potential energy $U(\vec{r})$ can be mapped out in many situations. An estimate of such potentials could be very important. If an accurate potential is at hand, the dynamics of a vortex in a nanodot might be described by a greatly reduced number of degrees of freedom. In certain situations, the dynamics of the vortex core can be described via an effective equation of motion[44] with a vortex gyrovector $\vec{G}$ and mass tensor $\tilde{\mathcal{M}}$. The potential $U(\vec{r})$ determines the force $\vec{F} = -\vec{\nabla}U(\vec{r})$ in the equation of motion for the core position $[\vec{V} = \dot{\vec{X}}(t)$,

$$\vec{F} + \vec{G} \times \vec{V} = \tilde{\mathcal{M}} \cdot \frac{d\vec{V}}{dt}. \tag{1}$$

A knowledge of the potential and hence the force could be used to predict and analyze the vortex dynamics in a dot.

For determining the potential, calculations are carried out for the parameters of Permalloy-79 ($\mathrm{Fe}_{21}\mathrm{Ni}_{79}$), which has saturation magnetization $M_S = 860$ kA/m, continuum exchange stiffness $A = 13$ pJ/m, Curie temperature near 630 K, and face-centered-cubic lattice structure with conventional unit cell parameter $a_0 = 0.355$ nm.

II. VORTEX PROPERTIES

Based on the properties of vortices in a pure circular magnetic dot without defects, we can extend the discussion to problems with defects. In general, the magnetization can be described by in-plane angles Φ_i and the out-of-plane component, M_i^z, where i refers to cells used to partition the system. For a defect-free dot of adequate size, the vortex ground state can be described by giving the in-plane angles as

$$\Phi_i = \phi_i + \phi_0, \tag{2}$$

where $\phi_i = \tan^{-1}(y_i/x_i)$ is the azimuthal coordinate measured with respect to the dot center, and $\phi_0 = \pm 90^\circ$ is a constant global rotation of all the dipoles away from the radial direction. The vortex has two equivalent states at $\phi_0 = \pm 90^\circ$, corresponding to opposite directions of the rotation of the spins around the center of the dot. These two states have opposite circulation $C \approx \pm 1$, a quantity defined by the sum over the cells of the whole system,

$$C = \frac{1}{N} \sum_i \hat{m}_i \cdot \hat{\phi}_i. \tag{3}$$

If the dipoles tilt out of the xy-plane, this sum can be less than unity in magnitude. The switching of this degree of freedom of the vortex could be caused by an applied field,[45] or by a current through the dot.[46]

The out-of-plane component m_z is monotonically decreasing outward from the vortex core. An approximate analytic expression for m_z has been given (rigid vortex model)[47] and its switching between two degenerate states (i.e., the vortex polarization) is of considerable interest.[48,49] When a vortex is pinned into a hole, even for an extremely small hole the magnetization will remain essentially lying within the plane of the dot and there is no polarization. Thus, one can imagine design of devices with three possible polarization states (+1, 0, -1). For determination of vortex states numerically, we initiate a planar vortex into the system by using expression (2). During the relaxation iteration, a vortex not centered in a hole will develop nonzero m_z in its core region as it lowers its total energy. Any small asymmetry in the initial state can select which polarization state is eventually reached.

The vortex core location can be defined roughly as within the cell where the effective vorticity charge is concentrated, i.e., where the following integral around the cell edges gives $q = 1$:

$$q = \frac{1}{2\pi} \oint \vec{\nabla}\Phi \cdot d\vec{r}. \tag{4}$$

Due to the demagnetization energy, the vortex with $q = -1$ is unstable.

When a vortex is pinned on a hole or defect, there is a certain minimum input energy (or applied field) required just to pull the vortex out. An important goal of this work is to estimate the dependence of this threshold energy and field on the hole size and other parameters.

III. EFFECTIVE MICROMAGNETICS HAMILTONIAN

In the underlying atomic system, the spins have atomic magnetic dipole moments of magnitude $\mu_{\text{atom}} = g\mu_B S$, where g is the Landee g-factor, μ_B is the Bohr magneton, and S is the spin length. Assuming fcc lattice structure, there are four atoms per conventional unit cell of size a_0^3, giving a volume per atom of $v_1 = a_0^3/4$, and the saturation magnetization is

$$M_S = \frac{g\mu_B S}{v_1}. \tag{5}$$

(With the parameters for Py, this implies atomic dipole moments $\mu_{\rm atom} = 9.62 \times 10^{-24}$ A $\cdot$ m^2.)

From the micromagnetics viewpoint, the system is partitioned into cells, each containing many atoms, which are small enough that the net magnetic moment might have a nearly constant magnitude, but varying direction. The simulations need only keep track of the directions of the magnetic moments in each cell. Obviously it is an approximation. But if the exchange is strong enough, then the spins in a cell stay mostly aligned, hence the dipole moment in a cell has a nearly fixed length, equal to the saturation magnetization times the cell volume.

The cells being used do not have to be cubic. In a thin magnet, there is only weak dependence on z, the coordinate measuring distance through the thickness. The nano-disk has a radius R and thickness $L \ll R$. To a first approximation we can ignore any dependence of $\vec{M}$ on the longitudinal coordinate z. Then it makes sense to have cells which are small in xy directions, but longer columns in the z direction, and use only a single layer of cells. In this way the problem is converted into an equivalent two-dimensional problem. The working cells can be of dimensions $a \times a \times L$, where a is greater than the atomic lattice parameter a_0, and $L = la$ is the total thickness of the sample. To be appropriate from the physical point of view, however, L should be small enough, so that the assumption of spins aligned within a cell is still valid. The spins in a cell being aligned means the magnetization is assumed to be saturated in each cell. The cell edges are assumed to be smaller in the xy directions, where the magnetization changes more rapidly with position.

The volume of a working cell $v_{\rm cell} = La^2$ contains many atoms. Assuming the atoms fill an fcc lattice as for Permalloy, the number of atoms in a working cell must be $la^3/(a_0^3/4)$. Then the saturated magnetic moment $\mu_{\rm cell}$ in a cell would be

$$\mu_{\rm cell} = M_s v_{\rm cell} = M_s L a^2, \tag{6}$$

which can also be expressed as

$$\mu_{\rm cell} = \frac{g\mu_B S}{a_0^3/4} \times la^3 = 4l\left(\frac{a}{a_0}\right)^3 \mu_{\rm atom}. \tag{7}$$

For most of the studies here, we consider a Permalloy disk 12 nm thick, and use a cell size $a = 2.0$ nm. This results in $\mu_{\rm cell} = 2010\ \mu_{\rm atom}$. In the micromagnetics viewpoint, these will be taken as the fixed magnitude dipoles that interact with each other via local exchange and long-range dipolar forces. Computationally, we will follow their unit vectors $\hat{m}(\vec{r}) = \vec{\mu}(\vec{r})/\mu_{\rm cell}$. These only need to be defined on a two-dimensional grid, but we need to know their effective couplings.

A. Exchange interactions

We define the interactions between the cells, starting from the continuum magnetics Hamiltonian that includes exchange and demagnetization energies produced by magnetization $\vec{M}(\vec{r})$. Here it is assumed that local anisotropy is small. The exchange stiffness A is used to define the exchange energy based on the scaled continuum magnetization, $\vec{m} = \vec{M}/M_S$, through

$$\mathcal{H}_{\rm ex} = A \int dV\ \nabla\vec{m} \cdot \nabla\vec{m}. \tag{8}$$

For the exchange interactions, we use the general expression (8) converted to a finite difference representation on the chosen cell grid. Although the underlying atomic interactions live on the fcc lattice, those interactions are thought of as smoothed out, and now we just have the cell-to-cell exchange interactions. We assume a square cell grid (ignoring the z-dependence). A cell centered at the origin is surrounded by four other cells, at displacements of $\pm a\hat{x}$ and $\pm a\hat{y}$ (measured to their centers). Then the exchange energy of our cell at the origin interacting with only the two neighbors to the right and above, as a lowest order finite difference approximation to (8), is

$$\begin{aligned}\mathcal{H}_{\rm ex,cell} &= Av_{\rm cell} \times \left\{ \left(\frac{\vec{m}(a\hat{x}) - \vec{m}(0)}{a}\right)^2 \right.\\ &\qquad \left. + \left(\frac{\vec{m}(a\hat{y}) - \vec{m}(0)}{a}\right)^2 \right\}. \end{aligned} \tag{9}$$

We use only these two neighbors; then by summing over all cells, there will be no double counting, as every cell-to-cell bond will be included only once. Expanding and re-arranging, this becomes

$$\mathcal{H}_{\rm ex,cell} = \frac{Av_{\rm cell}}{a^2}\left\{4\vec{m}^2 - 2\vec{m}(0) \cdot [\vec{m}(a\hat{x}) + \vec{m}(a\hat{y})]\right\}. \tag{10}$$

But the magnetization vectors $\vec{M}$ that produce $\vec{m} = \vec{M}/M_S$ in each cell have been assumed to be saturated to the magnitude M_S. It means that the each $\vec{m}$ is a unit vector, so the per-cell exchange contribution is

$$\mathcal{H}_{\rm ex,cell} = \frac{2Av_{\rm cell}}{a^2}\left\{2 - \hat{m}(0) \cdot [\hat{m}(a\hat{x}) + \hat{m}(a\hat{y})]\right\}. \tag{11}$$

Finally, it can be expressed as the exchange energy per bond,

$$\mathcal{H}_{\rm ex,bond} = \frac{2Av_{\rm cell}}{a^2}\left[1 - \hat{m}(0) \cdot \hat{m}(a\hat{x})\right]. \tag{12}$$

It demonstrates that the effective exchange coupling between the cells (i.e., cell-to-cell) is

$$J_{\rm cell} = \frac{2Av_{\rm cell}}{a^2} = 2AL. \tag{13}$$

Dropping the irrelevant constant, the exchange Hamiltonian for the cells is

$$\mathcal{H}_{\rm ex} = -J_{\rm cell} \sum_{(i,j)} \hat{m}_i \cdot \hat{m}_j \tag{14}$$

where only interactions between nearest neighbor cells are included.

B. Dipolar interactions

The exchange strength between cells needs to be contrasted to the strength of their effective dipolar interactions. We already saw that each cell has a dipole moment of magnitude $\mu_{\rm cell} = (4la^3/a_0^3)\mu_{\rm atom}$. These interact as well according to the usual dipole-dipole interaction. Also, lengths (or positions) will be measured in units of the cell size, a, and it is convenient to use the unit vector magnetic moments, $\hat{m}_i = \vec{\mu}_i/\mu$, the discrete version of $\hat{m} = \vec{M}/M_S$. Thus we have the dipolar terms for micromagnetics calculations,

$$\mathcal{H}_{\rm dd} = -\frac{\mu_0}{4\pi}\frac{\mu_{\rm cell}^2}{a^3}\sum_{i>j}\frac{[3(\hat{m}_i\cdot\hat{r}_{ij})(\hat{m}_j\cdot\hat{r}_{ij}) - \hat{m}_i\cdot\hat{m}_j]}{(r_{ij}/a)^3} \tag{15}$$

However, we do not evaluate the dipolar energy this way, because it gets very slow for even moderate system size. Instead, we resort to finding the "stray field" or demagnetization field, which then interacts with the dipoles. We do this by a FFT solution of the effective magnetics equation, which gives the solution for magnetic potential Φ_M when a given magnetization distribution is provided. It is based on Gauss's law for the magnetic induction,

$$\vec{\nabla}\cdot\vec{B} = \mu_0(\vec{\nabla}\cdot\vec{H} + \vec{\nabla}\cdot\vec{M}) = 0. \tag{16}$$

We assume the magnetic field is derived from a potential, in the absence of free currents.

$$\vec{H}_M = -\vec{\nabla}\Phi_M, \quad \text{then} \quad -\nabla^2\Phi_M = -\vec{\nabla}\cdot\vec{M} \tag{17}$$

The RHS is an effective magnetic charge density, so we can write

$$-\nabla^2\Phi_M = \rho_M, \quad \text{where} \quad \rho_M = -\vec{\nabla}\cdot\vec{M} \tag{18}$$

Once the magnetic field is known, the demagnetization energy is known to be given by the expression,

$$\mathcal{H}_{\rm dd} = \mathcal{H}_{\rm demag} = -\frac{1}{2}\mu_0\int dV\ \vec{H}_M\cdot\vec{M} \tag{19}$$

The factor of 1/2 takes care of double counting of the field interactions. If there is also an externally applied magnetic field, then it makes an additional energy contribution,

$$\mathcal{H}_B = -\mu_0\int dV\ \vec{H}_{\rm ext}\cdot\vec{M} \tag{20}$$

$$\mathcal{H}_B = -\sum_i \vec{B}_{\rm ext}\cdot\vec{\mu}_i = -\mu_0 M_S\int dV\ \vec{H}_{\rm ext}\cdot\hat{m} \tag{21}$$

C. Units for Computations

To continue, it is convenient to use some dimensionless units, from which the definition of the magnetic exchange length emerges. Magnetization is already scaled by M_S to give the dimensionless form, $\hat{m}$. The gradient operator is scaled by the cell size, to give a dimensionless gradient,

$$\tilde{\vec{\nabla}} \equiv a\vec{\nabla} \tag{22}$$

This then leads to the dimensionless magnetic charge density $\tilde{\rho}$,

$$\rho_M = -\vec{\nabla}\cdot\vec{M} = -\frac{1}{a}\tilde{\nabla}\cdot(M_S\hat{m}) = \frac{M_S}{a}\tilde{\rho} \tag{23}$$

which means the definition is

$$\tilde{\rho} \equiv -\tilde{\vec{\nabla}}\cdot\hat{m} \tag{24}$$

Similarly there is the dimensionless magnetic potential, derived from $\tilde{\rho}$,

$$-\nabla^2\Phi_M = -\frac{1}{a^2}\tilde{\nabla}^2\Phi_M = -\frac{1}{a}\tilde{\nabla}\cdot(M_S\hat{m}) = \frac{M_S}{a}\tilde{\rho} \tag{25}$$

$$\Phi_M = aM_S\tilde{\Phi} \tag{26}$$

Then the dimensionless equation being solved computationally is

$$-\tilde{\nabla}^2\tilde{\Phi} = \tilde{\rho} \tag{27}$$

The demagnetization field is

$$\vec{H}_M = -\vec{\nabla}\Phi_M = -\frac{1}{a}\tilde{\nabla}(aM_S\tilde{\Phi}) = -M_S\tilde{\nabla}\tilde{\Phi} \tag{28}$$

Then it makes sense to define the dimensionless demagnetization field,

$$\tilde{H}_M = -\tilde{\nabla}\tilde{\Phi} \quad , \quad \vec{H}_M = M_S\tilde{H}_M, \tag{29}$$

which has an associated magnetic induction,

$$\vec{B}_M = \mu_0\vec{H}_M = -\mu_0 M_S\tilde{\nabla}\tilde{\Phi} = \mu_0 M_S\tilde{H}_M. \tag{30}$$

The most interesting result in dimensionless units is the demagnetization energy. A chosen magnetic dipole has that interaction expressed as

$$\begin{aligned} U_M = -\frac{1}{2}\vec{B}_M\cdot\mu_i &= -\frac{1}{2}\mu_0 M_S(-\tilde{\nabla}\tilde{\Phi})\cdot M_S v_{\rm cell}\,\hat{m}_i \\ &= -\frac{1}{2}\mu_0 M_S^2 La^2\,(\tilde{H}_M\cdot\hat{m}_i). \end{aligned} \tag{31}$$

But it is necessary to measure all energies in the same units. For this, we use units of the cell-to-cell exchange constant, $J_{\rm cell} = 2AL$. So we write

$$\begin{aligned} \frac{U_M}{J_{\rm cell}} &= -\frac{1}{2}\frac{\mu_0 M_S^2 La^2}{2AL}(\tilde{H}_M\cdot\hat{m}_i) \\ &= -\frac{1}{2}\left(\frac{a}{\lambda_{\rm ex}}\right)^2(\tilde{H}_M\cdot\hat{m}_i) \end{aligned} \tag{32}$$

where the exchange length is defined from

$$\lambda_{\rm ex} = \sqrt{\frac{2A}{\mu_0 M_S^2}}. \tag{33}$$

Similarly, if there is an externally applied magnetic field, the interaction energy is scaled in the same way,

$$\frac{U_B}{J_{\rm cell}} = -\left(\frac{a}{\lambda_{\rm ex}}\right)^2 (\tilde{H}_{\rm ext} \cdot \hat{m}_i) \tag{34}$$

where the external magnetic induction and field are related by

$$\vec{B}_{\rm ext} = \mu_0 \vec{H}_{\rm ext} = \mu_0 M_S \tilde{H}_{\rm ext} \tag{35}$$

D. Dimensionless Hamiltonian and Effective Field

Combining the interactions in dimensionless form, involving the unit vector moments $\hat{m}_i = \vec{\mu}_i/\mu_{\rm cell}$, we have the total Hamiltonian for the micromagnetics cells

$$\begin{aligned}\mathcal{H}_{\rm mm} &= -J_{\rm cell}\left\{\sum_{(i,j)} \hat{m}_i \cdot \hat{m}_j \right. \\ &\left. + \left(\frac{a}{\lambda_{\rm ex}}\right)^2 \sum_i \left(\tilde{H}_{\rm ext} + \frac{1}{2}\tilde{H}_M\right) \cdot \hat{m}_i\right\}. \end{aligned} \tag{36}$$

This is associated with the effective magnetic field on a site,

$$\begin{aligned}\vec{F}_i &= -\frac{\partial \mathcal{H}_{mm}}{\partial \hat{m}_i} \\ &= J_{\rm cell}\left\{\sum_{\rm nbrs} \hat{m}_j + \left(\frac{a}{\lambda_{\rm ex}}\right)^2 \left(\tilde{H}_{\rm ext} + \frac{1}{2}\tilde{H}_M\right)\right\}. \end{aligned} \tag{37}$$

This field determines both the total system energy, and applies to the undamped dynamics when the gyromagnetic ratio $\gamma \approx -e/m_e$ is included into the torque equation:

$$\mathcal{H}_{mm} = -\sum_i \vec{F}_i \cdot \hat{m}_i, \tag{38}$$

$$\dot{\hat{m}}_i = \gamma_i \hat{m}_i \times \vec{F}_i. \tag{39}$$

In the work here, we do not actually use time dynamics, so the gyromagnetic ratio is not needed. But the effective fields $\vec{F}_i$ do determine the energetics, and we use them to find local energy minima.

The simulations were performed for circular Permalloy disks from 80 nm to 240 nm diameter, similar is size to samples used in recent experiments. We used a cell size of $a = 2.0$ nm, and two different disk thicknesses $L = la = 12$ nm and $L = 4.0$ nm, with exchange stiffness $A = 13$ pJ/m and exchange length $\lambda_{\rm ex} = 5.3$ nm, as found in Py.

IV. THE DEMAGNETIZATION FIELD $\tilde{H}_M$ IN A THIN SAMPLE

The solution of the Poisson equation (27) is effected by a Green's function,

$$\tilde{\Phi}(\vec{r}) = \int d^3r'\; G(\vec{r},\vec{r}')\,\tilde{\rho}(\vec{r}') = \int G(\vec{r},\vec{r}')\,dq' \tag{40}$$

where $dq' = dq(\vec{r}')$. The charge density may include parts on the surfaces that appear more as a surface charge density,

$$\tilde{\sigma} = \hat{m} \cdot \hat{n} \tag{41}$$

where $\hat{n}$ is the outward normal from the system. The system is assumed to be a thin cylinder. The magnetization is assumed to depend only on x and y, not on the vertical coordinate, z. Then there are surface charges $\tilde{\sigma}_z = \pm\hat{m}_z$ on the upper and lower planar (circular) faces of the dot, respectively. There can be additional surface charges along the curved edge of the cylinder. In this section we drop the M subscript on $\tilde{H}_M$. It is understood we are discussing only the demagnetization field.

The 3D Green's function for the Poisson equation is

$$G(\vec{r},\vec{r}') = \frac{1}{4\pi|\vec{r}-\vec{r}'|} \tag{42}$$

Specializing to a thin system with $L \ll R$ leads to effective Green's functions for a two-dimensional problem.[40] We summarize the approach here to exhibit the special treatment given to the results near the origin, $|\vec{r}-\vec{r}'| \to 0$.

A. Finding the longitudinal field component $\tilde{H}_z$

The contributions to $\tilde{H}_z$ come only from the charges on the upper and lower planar faces. Let the coordinate z of the observation point lie inside the range between $-\delta \le z \le +\delta$, where $\delta = L/2$. From the area element $dA' = dx'\, dy'$, where $dq' = \sigma' dA' = \hat{m} \cdot \hat{n}\; dx'\, dy'$, we get

$$d\tilde{\Phi}(x,y,z) = \frac{dA'}{4\pi}\left\{\frac{m_z}{\sqrt{r^2+(z-\delta)^2}} + \frac{-m_z}{\sqrt{r^2+(z+\delta)^2}}\right\} \tag{43}$$

where $r^2 \equiv (x-x')^2 + (y-y')^2$. The gradient w.r.t. z gives the field increment produced,

$$\begin{aligned} d\tilde{H}_z &= -\frac{\partial}{\partial z}(d\tilde{\Phi}) \\ &= -\frac{dA'}{4\pi}\left\{\frac{-m_z(z-\delta)}{(r^2+(z-\delta)^2)^{3/2}} + \frac{m_z(z+\delta)}{(r^2+(z+\delta)^2)^{3/2}}\right\} \end{aligned} \tag{44}$$

At the center of the sample, $z = 0$, we would get the net demagnetization field there by integrating over all elements,

$$\tilde{H}_z(0) = \int dx'\, dy'\; \left\{\frac{-1}{4\pi}\frac{2\delta}{[r^2+\delta^2]^{3/2}}\right\} m_z(x',y'). \tag{45}$$

The factor within braces is an effective Green's function, used to get the demagnetization field in the middle of the cylinder. We might call it G_0, it is understood that it gives $\tilde{H}_z(0)$.

$$\tilde{H}_z(0) = \int dx'\, dy'\, G_0(r)\ m_z(x',y') \tag{46}$$

$$\begin{aligned} G_0(r) &= \frac{-1}{4\pi} \frac{2\delta}{[r^2+\delta^2]^{3/2}}, \\ r^2 &= (x-x')^2 + (y-y')^2. \end{aligned} \tag{47}$$

To get a better approximation for total magnetic energy, we instead need the average demagnetization field over the whole range of z (average in a cell). So we find instead the vertical field component averaged over all z, denoted just as $\tilde{H}_z$,

$$d\tilde{H}_z = \frac{1}{2\delta}\int_{-\delta}^{\delta} dz\, \left(\frac{-\partial}{\partial z} d\tilde{\Phi}\right) = \frac{-1}{2\delta}\ d\tilde{\Phi}\Big|_{-\delta}^{+\delta} \tag{48}$$

Then using Eq. (43) and including the integration over x' and y' gives

$$\begin{aligned} \tilde{H}_z &= \int dx'\, dy'\ d\tilde{H}_z \\ &= \int dx'\, dy' \left\{ \frac{1}{4\pi\delta}\left[\frac{1}{\sqrt{r^2+(2\delta)^2}} - \frac{1}{r}\right]\right\} m_z(x',y'). \end{aligned} \tag{49}$$

The part in braces is a Green's function; call it G_z. It gives the average vertical field at some point (x,y). It is better to write G_z and the above relationship using the two-dimensional vectors $\tilde{r}=(x,y)$ and $\tilde{r}\,'=(x',y\,')$, and using the dot thickness L, as a convolution,

$$\tilde{H}_z(\tilde{r}) = \int d^2\tilde{r}\,'\ G_z(\tilde{r}-\tilde{r}\,')\ m_z(\tilde{r}\,') \quad , \quad \tilde{r} \equiv (x,y) \tag{50}$$

$$G_z(\tilde{r}) = \frac{1}{2\pi L}\left[\frac{1}{\sqrt{\tilde{r}^2+L^2}} - \frac{1}{|\tilde{r}|}\right] \quad , \quad \tilde{r}^2 \equiv x^2+y^2 \tag{51}$$

B. Finding the in-plane demagnetization field components.

The volume charge density (together with some surface charges at the curved boundary of the cylinder) will produce the in-plane field components. From the basic Green's function (42) for the Poisson equation look at the contribution to potential at (x,y,z) caused by the volume charge density at (x',y'), as $\tilde{\rho}$ does not depend on z'. This involves an integration over source points z', for the contribution from charge $dq\,' = \tilde{\rho}(x',y')\ dx\,'dy\,'$,

$$d\tilde{\Phi}(x,y,z) = \left\{\frac{1}{4\pi}\int_{-\delta}^{+\delta} dz\,' \frac{1}{\sqrt{r^2+(z-z\,')^2}}\right\} dq\,' \tag{52}$$

where $r^2 \equiv (x-x')^2 + (y-y')^2$. The integration is straightforward and leads to a well known result, one form of which is

$$d\tilde{\Phi}(x,y,z) = \frac{1}{4\pi}\ln\left[\frac{\sqrt{r^2+(\delta-z)^2}+\delta-z}{\sqrt{r^2+(\delta+z)^2}-\delta+z}\right] dq\,' \tag{53}$$

As this depends on the vertical position, it is necessary to average it over z. In terms of the dot thickness $L=2\delta$, the averaging is

$$\begin{aligned} d\tilde{\Phi}(x,y) &= \frac{1}{2\delta}\int_{-\delta}^{\delta} dz\ d\tilde{\Phi}(x,y,z) \\ &= \frac{1}{2\pi L}\left[L\sinh^{-1}\left(\frac{L}{r}\right) + r - \sqrt{r^2+L^2}\right] dq\,' \end{aligned} \tag{54}$$

Because the result only depends on the radial distance of the observation point from the source point, only a radial demagnetization component is produced. The increment produced is

$$d\tilde{H}_r = -\hat{e}_r \frac{\partial}{\partial r}\left(d\tilde{\Phi}\right) = \frac{\hat{e}_r}{2\pi L}\left[\sqrt{1+\left(\frac{L}{r}\right)^2} - 1\right] dq\,'. \tag{55}$$

Thus the vector Green's function for the in-plane field is

$$\vec{G}_{xy}(\tilde{r}) = \frac{\hat{e}_{\tilde{r}}}{2\pi L}\left[\sqrt{1+\left(\frac{L}{\tilde{r}}\right)^2} - 1\right]. \tag{56}$$

This determines the (x,y) demagnetization field components as a convolution,

$$\tilde{H}_{xy}(\tilde{r}) = \int d^2\tilde{r}\,'\ \vec{G}_{xy}(\tilde{r}-\tilde{r}\,')\ \tilde{\rho}(\tilde{r}\,'). \tag{57}$$

The integration involves the unit vector between source and observation points,

$$\hat{e}_{\tilde{r}-\tilde{r}\,'} = \frac{\tilde{r}-\tilde{r}\,'}{|\tilde{r}-\tilde{r}\,'|}. \tag{58}$$

C. Finite difference approximations for magnetic charges

To apply Eq. (57), we use simple formulas to approximate the magnetic charge densities, both in the volume and at the curved surface. A surface site is any site of the 2D grid with less than 4 neighbors (for a square grid). As long as a site has four neighbors, it must be a volume site, then it only has volume charge density, defined from its charge,

$$q_M^{\rm vol} = -\int d^3x\ \vec{\nabla}\cdot\hat{m} = -\int \hat{m}\cdot d\vec{A} \tag{59}$$

For calculation of $\tilde{H}_{\text{xy}}$, one can ignore the top and bottom cell surfaces (at $z = \pm\delta$), whose charges cancel. This leaves only the edge terms,

$$\begin{aligned} q_M^{\text{vol}} &= -\left\{\hat{m}_{01}\cdot\hat{x} - \hat{m}_{03}\cdot\hat{x} + \hat{m}_{02}\cdot\hat{y} - \hat{m}_{04}\cdot\hat{y}\right\}(aL) \\ &= -\frac{1}{2}aL\left[m_1^x - m_3^x + m_2^y - m_4^y\right] \end{aligned} \tag{60}$$

where the values averaged between two cells are defined like

$$\hat{m}_{ij} \equiv \frac{1}{2}(\hat{m}_i + \hat{m}_j). \tag{61}$$

The notation is that "0" is a central cell, and 1,2,3,4 are located at displacements of $a\hat{x}$, $a\hat{y}$, $-a\hat{x}$ and $-a\hat{y}$ from the central cell, respectively. Then the contribution to charge density at the central cell is this divided by the cell volume,

$$\tilde{\rho}_0^{\text{vol}} = \frac{q_M^{\text{vol}}}{La^2} = -\frac{1}{2a}\left[m_1^x - m_3^x + m_2^y - m_4^y\right] \tag{62}$$

For the surface sites, we also need to include an extra amount of charge, the surface charge,

$$q_M^{\text{sur}} = \frac{1}{2}\hat{m}\cdot\vec{A} = \frac{aL}{2}\hat{m}\cdot\hat{n}, \tag{63}$$

that produces an additional contribution to charge density,

$$\tilde{\rho}_0^{\text{sur}} = \frac{q_M^{\text{sur}}}{La^2} = \sum_{\text{cell edges}} \frac{1}{2a}\hat{m}_0\cdot\hat{n}_{\text{edge}} \tag{64}$$

Associated in each cell we use the total charge found there, equally whether surface or volume charge. Note that these charges only determine the in-plane demagnetization components, $\tilde{H}_x, \tilde{H}_y$. The m_z component determines the out-of-plane demagnetization field, $\tilde{H}_z$.

D. Treatment of the 2D Green's functions near $r = 0$

When applied to the discretized system for micromagnetics, some care is needed in using the Green's functions near the origin, $|\tilde{r} - \tilde{r}\,'| \to 0$. We can let $\vec{G}_{\text{xy}} \to 0$ in this limit without difficulty. The Green's function for finding $\tilde{H}_z$ is singular at the origin; one sees $G_z(\tilde{r}) \sim \frac{1}{|\tilde{r}|}$. Therefore we make an approximation to G_z when we apply it on a grid with finite sized cells. (For simplicity, we drop the tilde notation for 2D vectors here.) Because its value exactly at $r = 0$ is undefined, we do an averaging of G_z over a circular region with the same area A_0 as a cell. That is, we average G_z out to a radius r_0 defined so that

$$A_0 = \pi r_0^2 = a^2 \quad , \quad r_0 = \frac{a}{\sqrt{\pi}} \tag{65}$$

Using the definition (51), the averaged value from $r = 0$ out to $r = r_0$ is

$$\begin{aligned} \langle G_z\rangle_0^{r_0} &= \frac{1}{a^2}\int_0^{r_0} 2\pi r\; dr\; G_z(r) \\ &= \frac{1}{La^2}\left[\sqrt{r_0^2 + L^2} - L - r_0\right] \end{aligned} \tag{66}$$

This is the non-divergent value to use in the origin cell. G_z can also be smoothed out on the grid in some of the cells surrounding the origin. We can do an averaging in the next layers of cells at $r = a$ and at $r = \sqrt{2}a$, again defining averaging radii according to area mapping. There are four cells that are nearest neighbors to the origin cell, at $r = a$, and we use the average of G_z between $r = r_0$ and $r = r_1$, the latter defined by

$$A_1 = \pi r_1^2 = a^2 + 4a^2 \quad , \quad r_1 = \sqrt{\frac{5}{\pi}}\,a \tag{67}$$

We also define an outer radius for the third set of cells at $r = \sqrt{2}a$, the four next-nearest neighbors,

$$A_2 = \pi r_2^2 = a^2 + 4a^2 + 4a^2 \quad , \quad r_2 = \sqrt{\frac{9}{\pi}}\,a \tag{68}$$

In these cells we use the averages (per cell) between two radii, like

$$\langle G_z\rangle_{r_0}^{r_1} = \frac{1}{2\pi L}\left[\left\langle\frac{1}{\sqrt{r^2+L^2}}\right\rangle - \left\langle\frac{1}{r}\right\rangle\right]_{r_0}^{r_1} \tag{69}$$

which means we need the averages,

$$\begin{aligned} \left\langle\frac{1}{r^2+L^2}\right\rangle_{r_0}^{r_1} &= \frac{1}{4a^2}\int_{r_0}^{r_1} dr\; 2\pi r\; \frac{1}{\sqrt{r^2+L^2}} \\ &= \frac{2\pi}{4a^2}\left[\sqrt{r_1^2+L^2} - \sqrt{r_0^2+L^2}\right] \end{aligned} \tag{70}$$

$$\left\langle\frac{1}{r}\right\rangle_{r_0}^{r_1} = \frac{1}{4a^2}\int_{r_0}^{r_1} dr\; 2\pi r\; \frac{1}{r} = \frac{2\pi}{4a^2}(r_1 - r_0) \tag{71}$$

Combining these gives the result

$$\langle G_z\rangle_{r_0}^{r_1} = \frac{1}{4La^2}\left[\sqrt{r_1^2+L^2} - \sqrt{r_0^2+L^2} - (r_1 - r_0)\right] \tag{72}$$

Inserting the specific values for the radii, gives these replacements in the region around the origin,

$$G_z(0) \longrightarrow \langle G_z\rangle_0^{r_0} = \frac{1}{La^2}\left[\sqrt{L^2+\frac{a^2}{\pi}} - L - \sqrt{\frac{a^2}{\pi}}\right] \tag{73}$$

$$G_z(a) \longrightarrow \langle G_z\rangle_{r_0}^{r_1} = \frac{1}{4La^2}\left[\sqrt{L^2+\frac{5a^2}{\pi}} - \sqrt{L^2+\frac{a^2}{\pi}} - \sqrt{\frac{5a^2}{\pi}} + \sqrt{\frac{a^2}{\pi}}\right] \tag{74}$$

$$G_z(\sqrt{2}\,a) \longrightarrow \langle G_z\rangle_{r_1}^{r_2} = \frac{1}{4La^2}\left[\sqrt{L^2+\frac{9a^2}{\pi}} - \sqrt{L^2+\frac{5a^2}{\pi}} - \sqrt{\frac{9a^2}{\pi}} + \sqrt{\frac{5a^2}{\pi}}\right] \tag{75}$$

When the Green function is used on a square grid, these are used in place of the exact expression. It avoids the divergence at the origin and gives reasonably good values for solution for $\tilde{H}$ in a uniformly magnetized circular cylinder as a test case.

E. FFT solution for the demagnetization field $\tilde{H}_M$

The expressions for $\tilde{H}_z$ and $\tilde{H}_x, \tilde{H}_y$ involve convolutions of the Green's functions with each appropriate source density. These convolutions in real space become direct multiplications of the corresponding space Fourier transforms when the operations are done in Fourier space. Expressions (50) and (57) were evaluated using 2D fast Fourier transforms on a square grid with a size $N_x \times N_x$, where $N_x = 2^p$ and p is an integer. N_x is chosen to be at least twice as large as the number of cells needed to fit across the dot diameter $D = 2R$. Stated otherwise, $N_x a \geq 2R$. The extra cells are needed to avoid the wraparound problem, so that the demagnetization field being found is that of an isolated nanodot without the periodicity effects of the FFT. Then for a given configuration of the cells' magnetic dipoles and the demagnetization field they produce, the total system energy is evaluated via the Hamiltonian (36).

V. CONSTRAINED VORTEX SOLUTIONS

We want to find solutions to the equations of motion under specific constraints that localize a vortex in a desired position. Without a constraint, vortex solutions can be found by damped Landau-Lifshitz-Gilbert dynamics, but the vortex will always move to its minimum energy position. So the constraint approach is necessary if we want to map out the effective potential experienced by a vortex. This can be done, for example, by using a constraining procedure like that in Ref. 43, where energy minimization is carried out while fixing the in-plane angles Φ_i of a set of "core" dipoles that are nearest to the desired vortex position. During an energy minimization, those core sites are allowed only to tilt out of the xy-plane, but not allowed to rotate within that plane. The disadvantage of that approach is no information is obtained about the force or effective field that is needed to secure a vortex in its desired position.

Here, instead we use a Lagrange multiplier scheme, exactly so that information about the constraining force and effective field is obtained. The basic idea is still to consider some number N_c of central core dipoles around the vortex center. We have considered from four to 96 core sites nearest to the desired vortex location. The procedure described here works best when the diameter of the core region is at least as large as the magnetic exchange length. We do an energy minimization that satisfies the unit-length constraint of the cell dipoles, and include another constraint for vortex position.

A. Constrained dipole lengths

Before introducing the position constraint, consider how Lagrange undetermined multipliers works. If we just wanted to constrain the dipole lengths to some value m, we use the energy $\mathcal{H}_{mm} = E[\vec{m}_i]$ as defined in (36) or in (38) to make a functional to be minimized,

$$\Lambda[\vec{m}_i] = E[\vec{m}_i] + \sum_i \alpha_i(\vec{m}_i^2 - m^2) \tag{76}$$

where the α_i are Lagrange multipliers. The $\vec{m}_i$ are non-unit vector dipoles; we consider variations in their components, m_i^β, $\beta = x, y, z$, so that E is minimized consistent with the constraint. The minimization follows from

$$\frac{\partial \Lambda}{\partial \alpha_i} = \vec{m}_i^2 - m^2 = 0 \tag{77}$$

$$\frac{\partial \Lambda}{\partial m_i^\beta} = \frac{\partial E}{\partial m_i^\beta} + 2\alpha_i m_i^\beta = 0, \qquad \beta = x, y, z \tag{78}$$

From the energy function (38), the gradients with respect to dipole components produce the local effective fields $\vec{F}_i$ displayed in (37), and

$$-F_i^x + 2\alpha_i m_i^\beta = 0. \tag{79}$$

Then the solution for the dipole components is

$$m_i^\beta = \frac{F_i^\beta}{2\alpha_i}. \tag{80}$$

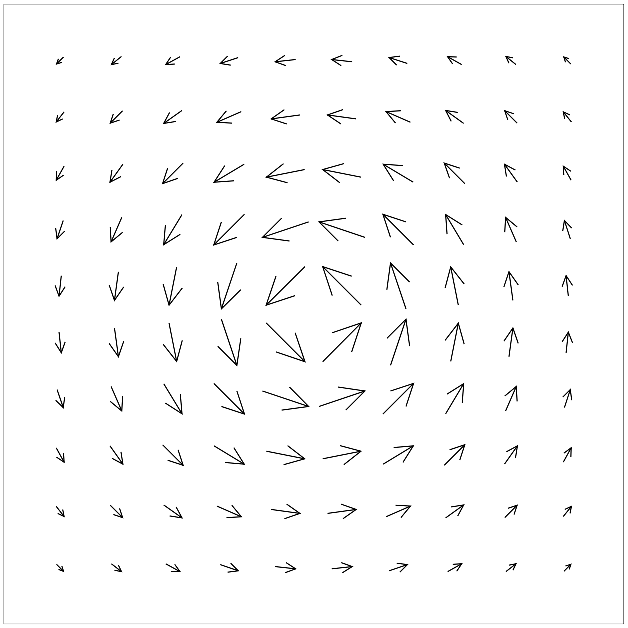

FIG. 1: Behavior of cell dipoles around a vortex core, with cell size $a = 2.0$ nm. The arrows' lengths in this view are proportional to each cell's out-of-plane magnetization component, m_z. Spatial variations in m_z occur over an exchange length $\lambda_{\rm ex} = 5.3$ nm.

When combined with the length constraint we get

$$\begin{aligned} \vec{m}_i^2 &= \frac{1}{4\alpha_i^2}[(F_i^x)^2 + (F_i^y)^2 + (F_i^z)^2] = m^2, \\ \alpha_i &= \frac{1}{2m}\left|\vec{F}_i\right|. \end{aligned} \tag{81}$$

Then the iteration algorithm to minimize the energy, while satisfying the length constraint, would be

$$m_i^\beta = m\frac{F_i^\beta}{|\vec{F}_i|}. \tag{82}$$

This is the usual "local field relaxation" algorithm for energy minimization, scaling to unit lengths, $m = 1$. Each dipole is placed along the direction of the effective field acting on it, and the process is repeated iteratively until a desired precision is achieved. It was used in Ref. 43, although not developed there by the Lagrange technique.

B. Constrained vortex core position

The vortex core position can be controlled by including an additional constraint. As a first approximation, with $N_c = 4$ core cells symmetrically located around the core position (Fig. 1), the core dipoles are assumed to satisfy a constraint

$$\sum_{i=1}^{N_c} m_i^x = \sum_{i=1}^{N_c} m_i^y = 0 \tag{83}$$

This would hold if a vortex is centered at the common corner of the four grid cells, see Figure 1. This term is included to make a new functional, applied when using N_c core sites (where N_c may be greater than four):

$$\Lambda[\vec{m}_i] = E[\vec{m}_i] + \sum_i \alpha_i(\vec{m}_i^2 - m^2) - \vec{\lambda}\cdot\sum_{n=1}^{N_c}\vec{m}_n \tag{84}$$

The new Lagrange multiplier $\vec{\lambda}$ is a vector with only x and y components. Now the minimization equations (in the core region) are

$$\begin{aligned} \frac{\partial \Lambda}{\partial m_n^x} &= \frac{\partial E}{\partial m_n^x} + 2\alpha_n m_n^x - \lambda_x = 0 \\ \frac{\partial \Lambda}{\partial m_n^y} &= \frac{\partial E}{\partial m_n^y} + 2\alpha_n m_n^y - \lambda_y = 0 \\ \frac{\partial \Lambda}{\partial m_n^z} &= \frac{\partial E}{\partial m_n^z} + 2\alpha_n m_n^z = 0 \end{aligned} \tag{85}$$

The results inside the core are

$$\begin{aligned} -F_n^x + 2\alpha_n m_n^x - \lambda_x &= 0 \quad \longrightarrow \quad m_n^x = \frac{1}{2\alpha_n}(F_n^x + \lambda_x) \\ -F_n^y + 2\alpha_n m_n^y - \lambda_y &= 0 \quad \longrightarrow \quad m_n^y = \frac{1}{2\alpha_n}(F_n^y + \lambda_y) \\ -F_n^x + 2\alpha_n m_n^z &= 0 \quad \longrightarrow \quad m_n^z = \frac{1}{2\alpha_n}F_i^z \end{aligned} \tag{86}$$

The constraint is just an extra magnetic field, applied only in the core cells. To complete the solution, one needs to determine that field. That comes from using the spin length constraint,

$$\vec{m}_n^2 = \frac{1}{4\alpha_n^2}\left[(F_n^x + \lambda_x)^2 + (F_n^y + \lambda_y)^2 + (F_n^z)^2\right] = m^2, \tag{87}$$

which gives

$$\frac{1}{\alpha_n} = \frac{2m}{\sqrt{(F_n^x + \lambda_x)^2 + (F_n^y + \lambda_y)^2 + (F_n^z)^2}}. \tag{88}$$

The constraint (83) also has to be applied to make the solution complete. Doing the sums in the core,

$$\sum_{\rm core} m_n^\beta = \sum_{\rm core}\frac{1}{2\alpha_n}(F_n^\beta + \lambda_\beta) = 0, \tag{89}$$

this leads to (for $\beta = x, y$ only)

$$\lambda_\beta = -\frac{\sum_{\rm core} F_n^\beta/\alpha_n}{\sum_{\rm core} 1/\alpha_n}. \tag{90}$$

Now we can see the algorithm for spin update is fairly simple. Initially, $\vec{\lambda}$ is set to zero. On each iteration step the new value of $\vec{\lambda}$ is found from expressions (88) and (90). Then do

$$\vec{m}_n = m\frac{(F_n^x + \lambda_x)\hat{x} + (F_n^y + \lambda_y)\hat{y} + F_n^z\hat{z}}{\sqrt{(F_n^x + \lambda_x)^2 + (F_n^y + \lambda_y)^2 + (F_n^z)^2}}. \tag{91}$$

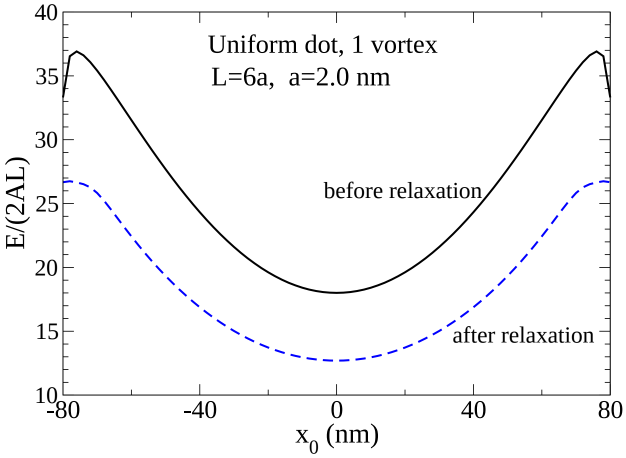

FIG. 2: (Color online) Result of the relaxation process for a vortex in a nanodisk of radius $R = 40a$, height $L = 6a$, using cell size $a = 2.0$ nm, $\lambda_{\rm ex} = 5.3$ nm, without applied field. The total disk energy in units of $J_{\rm cell} = 2AL$ is shown both before and after the converged relaxation, as a function of the constrained center position of the vortex. The "before" configuration consisted of a planar vortex; the relaxed configuration has an out-of-plane tilting of the magnetization at the vortex core.

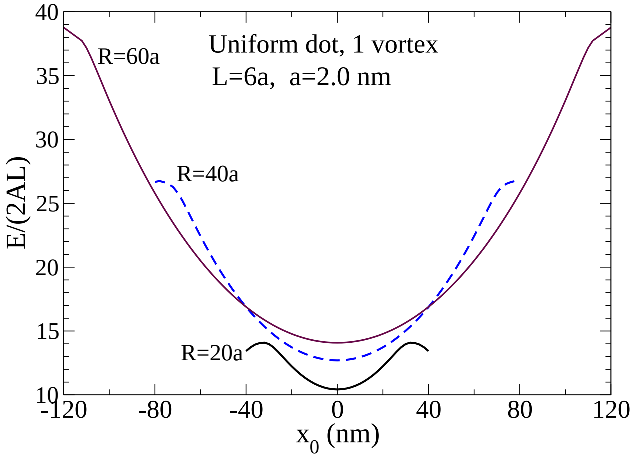

FIG. 3: (Color online) The relaxed vortex potentials for different disk radii as indicated, in disks of height $L = 6a = 12.0$ nm. x_0 is the horizontal displacement of the vortex core from the center. The potential is softer (lower force constant) but deeper in the wider disks.

By its design, the result is obviously of length m, which is set to $m = 1$. Further, it is clear that the spin solution must satisfy the position constraint (83). This is the basic vortex position algorithm.

It can be improved slightly, taking into account the possibility to constrain a vortex off-center in a cell, and also, to allow for out-of-plane tilting of the dipoles in the core. Instead of constraining the core sums to zero, suppose they are constrained to a value $\vec{T} = (T_x, T_y)$ that is set by the initial configuration, which is supposed to impose the desired position. The functional is modified to

$$\Lambda[\vec{m}_i] = E[\vec{m}_i] + \sum_i \alpha_i(\vec{m}_i^2 - m^2) - \vec{\lambda}\cdot\left(\sum_{core}\vec{m}_n - \vec{T}\right) \tag{92}$$

During the iteration, compute the nonzero sums

$$\sum_{\rm core} m_n^\beta = \sum_{\rm core}\frac{1}{2\alpha_n}\left(F_n^\beta + \lambda_\beta\right) = T_\beta \quad , \quad \beta = x, y. \tag{93}$$

The solution for the constraining field is now

$$\lambda_\beta = \frac{T_\beta - \sum_{\rm core} F_n^\beta/\alpha_n}{\sum_{\rm core} 1/\alpha_n}. \tag{94}$$

During iteration, the dipoles will tilt out of plane in the vortex core. So we consider that the constraining parameters T_x and T_y are moving constraints that change as the core dipoles tilt out of plane. As the iteration proceeds, T_x and T_y are continuously re-evaluated, according to a definition,

$$T_\beta = \left[\sum_{\rm core} m_n^\beta(0)\right]\left\langle\sqrt{1-(m_n^z/m)^2}\right\rangle, \tag{95}$$

where $\vec{m}_n(0)$ are from the original starting configuration, which give some values to define the core location. The m_n^z are the continuously changing out-of-plane components, increasing mainly near the vortex core. The square root factor gives the dipoles' projections into the xy-plane, which become smaller as the iteration proceeds. We use the average over the core region. If the vortex is centered in a unit cell, and the core region does not extend beyond the system edge nor into a hole, this new constraint has $T_x = T_y = 0$, reproducing constraint (83). Nonzero values of T_x or T_y only come into play when the vortex core is near an edge or hole in the system.

C. About the simulation parameters

The size of the core region is defined somewhat arbitrarily, using at least four cells, or other numbers such as $N_c = 12, 16, 24, 48, 96$, all of which give a symmetrical set of cells around a vortex located in the center of a unit cell. In most of our application, we used 24 core cells, defined as the ones closest to the desired vortex center. The cell size used was $a = 2.0$ nm, slightly smaller than the Permalloy exchange length $\lambda_{\rm ex} = 5.3$ nm.

In some cases the constraint produces particularly strong forces in the system. To avoid production of undesired solutions such as vortex-antivortex pairs, it is important that the diameter of the constrained region be larger than the magnetic exchange length. The N_c constrained cells have a total area $N_c a^2 = \pi r_c^2$, leading to

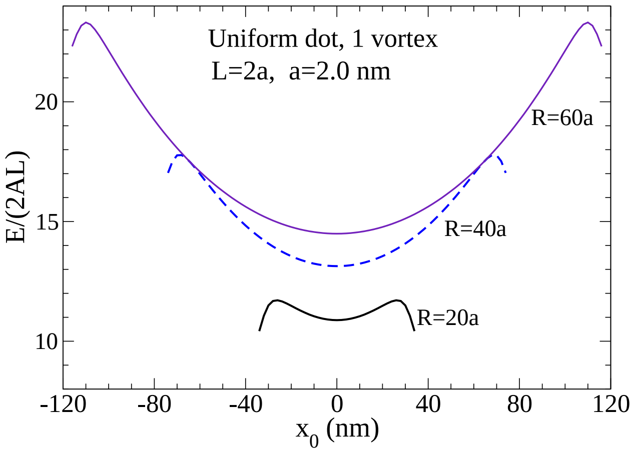

FIG. 4: (Color online) The relaxed vortex potentials for different disk radii as indicated, in very thin disks of height $L = 2a = 4.0$ nm. The potential is softer in these thin disks than in the thicker disks of Fig. 3, which makes it easier to move the vortex around by an applied external field.

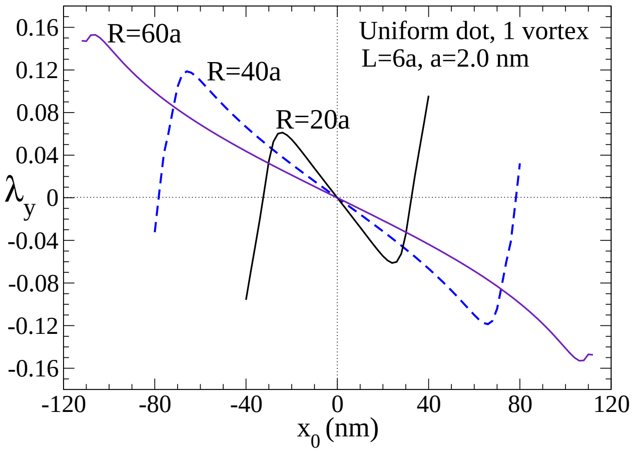

FIG. 5: (Color online) The constraining field λ_y needed to insure a desired vortex location $(x_0, 0)$, for the disks of height $L = 6a = 12.0$ nm whose potentials are shown in Fig. 3. The vortex has a positive rotation of the magnetic moments (i.e., counterclockwise viewed from above, $\phi_0 = +90^\circ$, or $C = +1$). When requiring a desired position $(x_0, 0)$ the constraining field must be in the perpendicular direction. The constraining field increases more slowly for the larger disks.

a constrained radius $r_c = \sqrt{N_c/\pi}\ a$. The process does result in a slight deformation of the vortex near its core. This is to be expected, because of the competition between the long-range forces acting on the vortex and the constraining forces applied on the core region. Relaxations that did not preserve the desired single vortex, usually due to very large forces, were thrown out from the results. These included vortex-free single-domain solutions at high applied fields and other configurations.

The applied and demagnetization fields in the Hamiltonian (36) and its extension $\Lambda[\vec{m}_i]$ in (92) appear multiplied by the factor $(a/\lambda_{\rm ex})^2$. In order to compare them to the position constraint field $\vec{\lambda}$ it makes sense to define the scaled external field used in the simulations,

$$\vec{h}_{\rm ext} = \frac{a^2}{\lambda_{\rm ex}^2}\tilde{H}_{\rm ext} = \frac{a^2}{\lambda_{\rm ex}^2}\frac{\vec{H}_{\rm ext}}{M_S}. \tag{96}$$

In the calculations we specify the values of $h = |\vec{h}_{\rm ext}|$. In this way, $\vec{\lambda}$ and $\vec{h}_{\rm ext}$ are in the same units. A similar transformation can also be defined for scaled demagnetization field. Indeed, this relation can be used in reverse to define a physical field strength $\vec{H}_\lambda$ that corresponds to the constraint field $\vec{\lambda}$ (switch $\vec{h}_{\rm ext}$ to $\vec{\lambda}$ on LHS and switch $\vec{H}_{\rm ext}$ to $\vec{H}_\lambda$ on RHS). For the simulations here, the ratio $\lambda_{\rm ex}^2/a^2 \approx 7.02$ is needed for the conversion from h_y to $H_{\rm ext}$ in units of M_S

VI. EFFECTIVE VORTEX-IN-DOT POTENTIALS

The approximate shape of the potential experienced by a vortex can be obtained through the zero-temperature

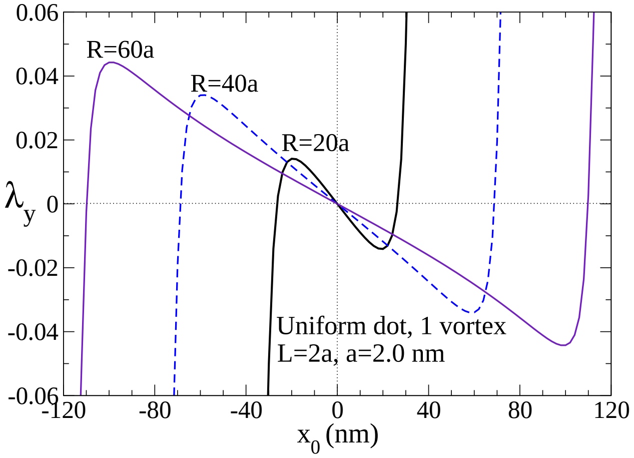

FIG. 6: (Color online) The constraining field λ_y needed to insure a desired vortex location $(x_0, 0)$, for the thinner disks of height $L = 6a = 12.0$ nm whose potentials are shown in Fig. 4. The vortex has a positive rotation of the magnetic moments (counterclockwise viewed from above). The constraining field needed is weaker than that in the thicker disks. The large nearly vertical sections are in unstable regions.

calculation of the total system energy described above, for a sequence of constrained vortex locations, $\vec{X} = (x_0, y_0)$. The origin $(0, 0)$ is the center of the disk; the vortex is "moved" along the x-axis, taking $y_0 = 0$. The energy minimization is carried out while artificially holding the vortex in place at position $\vec{X}$ via the constraining field $\vec{\lambda}$ that acts only on the N_c cells closest to the vortex

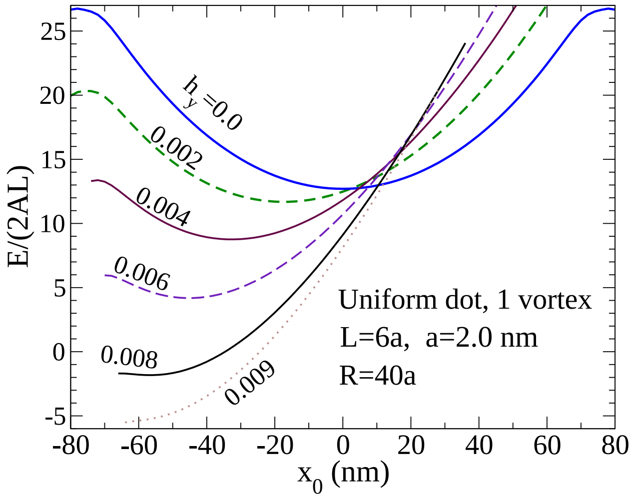

FIG. 7: (Color online) Relaxed vortex potentials for a disk of radius $R = 40a = 80.0$ nm, height $L = 6a = 12.0$ nm, in the presence of an externally applied field. The curves are labeled by the dimensionless scaled field h_y, that gives the physical field in units of saturation magnetization as $H_y = M_s(\lambda_{\rm ex}/a)^2 h_y$. The minimum-energy position shifts almost linearly with applied field. There is no vortex confined in the disk for when h_y surpasses ≈ 0.008 .

core. (Mostly we used $N_c = 24$.) The definition of core sites is rather liberal. If the vortex position $\vec{X}$ is somewhere inside a hole, then the N_c cells whose centers fall closest to $\vec{X}$ are considered the core, although they fall along the edge of the hole, and might be well-separated from $\vec{X}$ and from each other.

One iteration step involves changing all N cells. Typically hundreds or even thousands of iterations are required until the energy becomes accurate to 1 part in 10^7. The iteration was stopped when the average changes per iteration in the unit vector components ($\vec{m}$) fell below 10^{-7}, according to $\langle |\Delta m_x| + |\Delta m_y| + |\Delta m_z| \rangle < 10^{-7}$. Outside the core, all dipoles are completely free to move so as to lower their energy. Within the core, they move only as allowed by the Lagrange field $\vec{\lambda}$. The core obtains a slight shape deformation due to $\vec{\lambda}$.

A typical result for the system energy before and after the Lagrange constrained relaxation is shown in Fig. 2, for a disk of 160 nm diameter, 12 nm thick. The energy moves downward by about $5J_{\rm cell}$ due to the relaxation, while maintaining a potential very close to a parabolic shape, $U(x_0) = U_0 + \frac{1}{2}kx_0^2$.

A. Uniform cylindrical dots

Fig. 3 shows vortex-dot potentials for different sized dots of thickness $L = 6a = 12$ nm, not containing holes. The diameters are $D = 80$ nm, 160 nm, 240 nm. Fig. 4 shows the corresponding vortex-dot potentials in thinner dots, of thickness $L = 2a = 4$ nm. The vortex position was scanned across a diameter of the dot, $\vec{X} = (x_0, 0)$. The depth of the overall potential well increases with dot diameter and with dot thickness. There is a high relative potential near the dot's edge that stabilizes the vortex within the dot. If the dot is too small, the vortex destabilizes to a quasi-single-domain state. This can be attributed to the fact that the vortex potential well becomes flatter with reduced dot diameter.

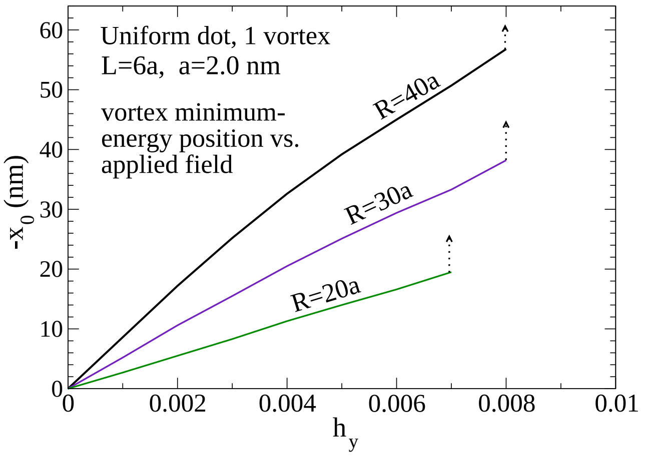

FIG. 8: (Color online) For disks of height $L = 6a = 12.0$ nm, the equilibrium vortex position (from Fig. 7) as a function of the applied field in scaled dimensionless form, h_y. The physical field in units of saturation magnetization is $H_y = M_s(\lambda_{\rm ex}/a)^2 h_y$. The curves are labeled by the disk radius. The upward arrows indicate the points beyond which there is no stable vortex solution in the nanodisk.

The corresponding constraining fields λ_y are displayed in Figures 5 and 6 for the two different dot thicknesses. The simulations were carried out for a vortex of positive circulation ($\phi_0 = +90°$ or $C = +1$). This requires a negative λ_y for a positive displacement x_0. When the vortex is near the disk center, the constraining field is proportional to x_0. For a vortex located far from the disk center, λ_y reverses, but this occurs in the unstable region where the vortex will not be naturally confined in the disk. One can see that λ_y changes sign at the same point where the potential has a local maximum near the disk edge. As expected from the form of the potentials, the thinner disks require a smaller constraining field, consistent with their smaller force constants.

For $x_0 < R/2$, the vortex potentials are very accurately fit by a parabolic form, $U(x_0) = U_0 + \frac{1}{2}kx_0^2$. The effective force constants for the two different disks thicknesses of 4.0 nm and 12.0 nm are displayed in Table I. The force constant decreases with increasing diameter, and increases with disk thickness. Typical values of this force constant for the disks studied, range from $k \sim 0.02A/a$ to $k \sim 0.4A/a$ or about 0.1 – 2.6 pN/nm in Py.

L	$R=20a$	$R=30a$	$R=40a$	$R=50a$	$R=60a$
$2a$	0.0502	0.0425	0.0339	0.0276	0.0228
$6a$	0.435	0.323	0.251	0.204	0.172

TABLE I: Values of the effective vortex-in-disk force constant k in units of exchange constant over cell size, A/a. The calculations used $a = 2.0$ nm.

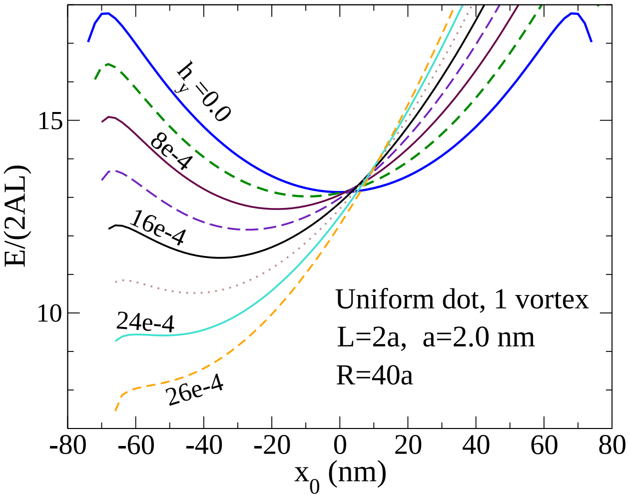

FIG. 9: (Color online) Relaxed vortex potentials for a thinner disk of radius $R = 40a = 80.0$ nm, height $L = 2a = 4.0$ nm, in the presence of an externally applied field. The curves are labeled by the dimensionless scaled field h_y. (Physical field $H_y = M_s(\lambda_{\text{ex}}/a)^2 h_y$.) The vortex is destabilized from the disk by only $h_y \approx 0.0024$.

B. Uniform cylindrical dot with an applied field

It is known that the application of an externally generated magnetic field $\vec{H}_{\text{ext}}$ tends to shift the vortex core position. This effect can be investigated by calculating the vortex potential. One example is shown in Fig. 7, for disks of 160 nm diameter and 12 nm thickness, where the potential is displayed for a range of applied fields in scaled form, h_y defined in Eqn. (96). The minimum of these potentials gives the equilibrium vortex position. Not surprisingly, the constraining field λ_y becomes zero at the vortex minimum energy position (not shown here). The minimum of the potential shifts to the left (towards $-\hat{x}$) with increasing applied field directed along the $\hat{y}$ axis (for positive circulation $C = +1$). For negative circulation, $C = -1$, field along $\hat{y}$ will result in displacement towards $+\hat{x}$. Eventually, at a field between $h_y = 0.008$ and $h_y = 0.009$, there is no minimum within the disk; the vortex is pushed out of the disk. For this example, the limiting field for a stable vortex $h_y \approx 0.008$ corresponds to a physical value $H_{\text{ext}} \approx 0.056 M_S$.

The vortex minimum energy position for different disk radii, all of thickness 12 nm, is displayed in Fig. 8. In each case the vortex is expelled from the disk at a limiting field that is a small fraction of the saturation magnetization. For small applied field, the vortex displacement varies linearly with applied field.

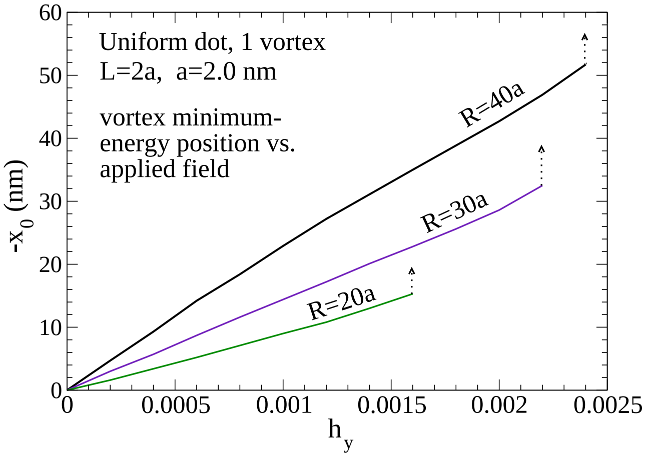

FIG. 10: (Color online) For thinner disks of height $L = 2a = 4.0$ nm and radii indicated, the equilibrium vortex position (from Fig. 9) as a function of the applied field in scaled dimensionless form, h_y. (Physical field is $H_y = M_s(\lambda_{\text{ex}}/a)^2 h_y$.) The thinner disks require a much lower field for removal of the vortex from the disk, which occurs at the upwards arrows.

If the disks are thinner, then consistent with their lower effective force constants, smaller applied field is required to displace the vortex from the disk center. The typical potentials for $R = 40a$ and $L = 2a = 4.0$ nm are shown in Fig. 9, for h_y ranging from 0.0 to 0.0026; the last value already expels the vortex from the disk. The limiting value for a vortex within the disk is around $h_y \approx 0.0024$ or $H_{\text{ext}} \approx 0.0168 M_S$. Fig. 10 displays the vortex minimum energy positions for these thinner disks. In terms of a susceptibility defined as the ratio of vortex position to applied field, $\beta = -x_0/(Ch_y)$, the susceptibility is higher in the thinner disks. Of course, the limiting fields are also considerably smaller in the thinner disks.

C. Cylindrical dot with a central hole

It is interesting to consider a cylindrical dot with a single central hole of radius R_h. A hole is simply a non-magnetic region with missing atoms or non-magnetic atoms. Although it may be somewhat artificial to specify the vortex location inside a hole, the procedure gives a reasonable view of the depth of the potential that a hole causes. Two cases are shown in Figs. 11 and 12, which exhibit the change in the dot potential for the two dot thicknesses and two different sized holes. One can see that the depth of the extra confining potential due to the hole increases dramatically with hole size. However, its depth does not depend significantly on the thickness of the dot. In a region out to a radius of about $3R_h$ the hole

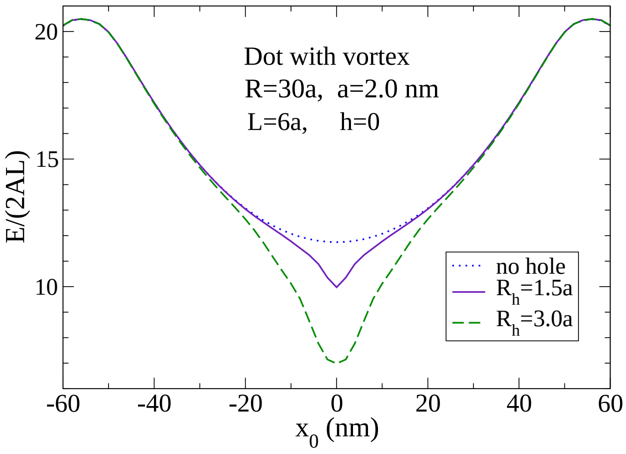

FIG. 11: (Color online) Relaxed vortex potentials for dots of radius $R = 30a = 60.0$ nm, height $L = 6a = 12$ nm, both without and with a central hole of radius R_h as indicated. The central hole provides a very strong confining potential.

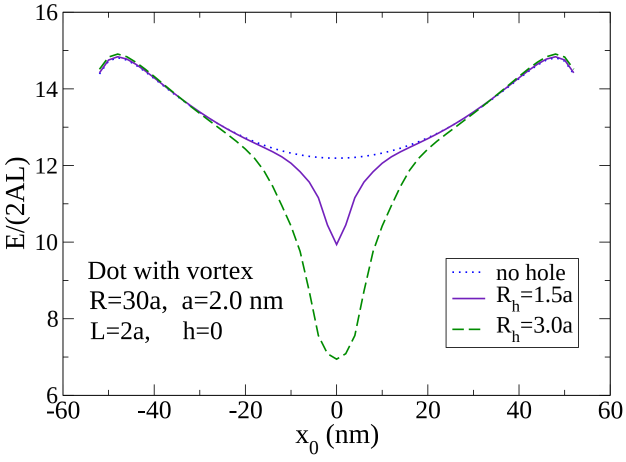

FIG. 12: (Color online) Relaxed vortex potentials for thin dots of radius $R = 30a = 60.0$ nm, height $L = 2a = 4.0$ nm, both without and with a central hole of radius R_h as indicated.

exerts a strong attractive force on the vortex, as seen by the steeper potential there. Far from the hole, however, there is little influence on the vortex and the potential follows the potential for the uniform dot.

D. Cylindrical dot with a central hole in applied field

For various reasons, it would be useful to estimate the applied field needed to pull a vortex out of a hole (threshold field). If the hole is a designed feature of the dot, then this can predict vortex stability with respect to field variations, or, give an estimate of the field required to liberate the vortex in a controlled way. Further, the threshold field could be important for vortex switching between pairs of holes.

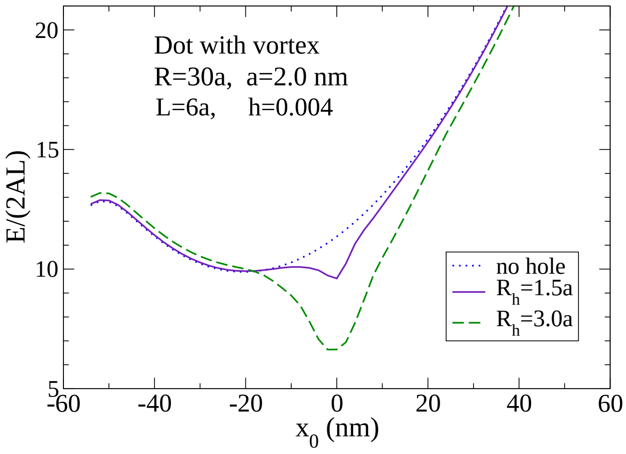

FIG. 13: (Color online) Relaxed vortex potentials for disks of radius $R = 30a = 60.0$ nm, height $L = 6a = 12$ nm, with applied field $h_y = 0.004$, both without and with a central hole of radius R_h as indicated. Note the two minima for the system with the smaller hole.

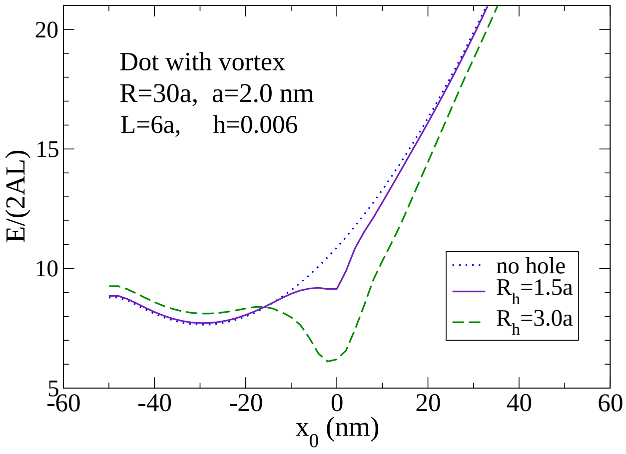

FIG. 14: (Color online) Relaxed vortex potentials for disks of radius $R = 30a = 60.0$ nm, height $L = 6a = 12$ nm, with applied field $h_y = 0.006$, both without and with a central hole of radius R_h as indicated. The minimum at the smaller hole has destabilized.

For dots with $R = 30a = 60$ nm, $L = 6a = 12$ nm, some vortex-dot potentials with applied field $h_y = 0.004$ are shown in Fig. 13, at the two holes sizes used above. For the smaller hole size, $R_h = 1.5a = 3.0$ nm, one sees that the vortex will be confined either in the hole or at a position $x_0 \approx -22$ nm, with only a very low potential barrier between the two states. Clearly this situation offers an opportunity for bistable operation between these two vortex states. For the larger sized hole,

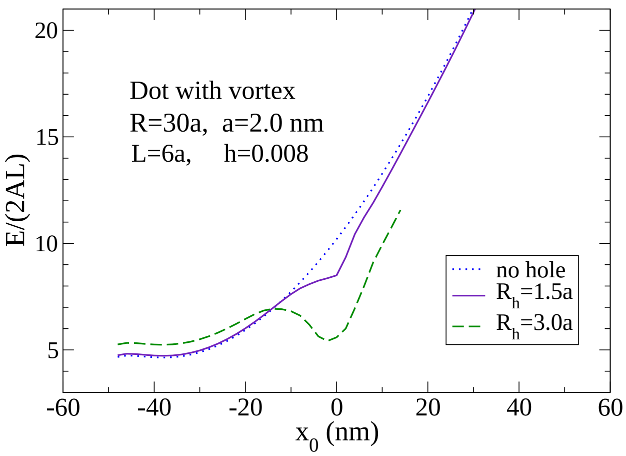

FIG. 15: (Color online) Relaxed vortex potentials for disks of radius $R = 30a = 60.0$ nm, height $L = 6a = 12$ nm, with applied field $h_y = 0.008$, both without and with a central hole of radius R_h as indicated. The system with the larger hole has two minima, however, the outer one is nearly unstable.

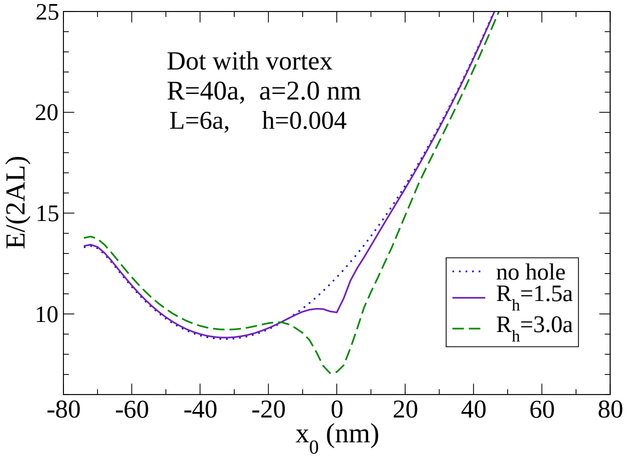

FIG. 16: (Color online) Relaxed vortex potentials for disks of radius $R = 40a = 80.0$ nm, height $L = 6a = 12$ nm, with applied field $h_y = 0.004$, both without and with a central hole of radius R_h as indicated. Here there two minima for both systems with different hole sizes.

$R_h = 3a = 6.0$ nm, the only stable minimum is when the vortex is confined in the hole. Upon increasing h_y, if the minimum at the hole disappears, then the threshold field has been surpassed.

If the applied field is increased to $h_y = 0.006$, as shown in Fig. 14, now the system with the smaller sized hole (3.0 nm radius) does not confine the vortex to the hole. Instead, the vortex has only the stable minimum near $x_0 \approx -30$ nm. Thus $h_y = 0.006$ is above the threshold field. One can see that a slight change in applied field should be able to switch the vortex reversibly between the hole-confined state and this other state about halfway out in the dot. At this same applied field, the dot with the larger radius hole (6.0 nm) now has acquired a minimum near $x_0 \approx -30$ nm, as well as the deeper minimum in the hole. However, the reversible switching might not be possible there, because the change in the shape of the potential with increasing field will destabilize the outer minimum before the minimum at the hole disappears. This is suggested in Fig. 15 where the results are shown for $h_y = 0.008$; the outer minimum is very weakly stable for both hole sizes there. A slight perturbation could cause the vortex to get expelled from the dot. Still, these results demonstrate the possibility for reversibly switching between a stable vortex within the dot and a quasi-single-domain vortex-free state. Note that the curves in these diagrams do not extend to $x_0 \to -R$ because those regions do not have stable vortex solutions.

The possibility for vortex-bistability can be improved by using a larger radius, $R = 40a = 80$ nm, as indicated in the potentials in Fig. 16, for $h_y = 0.004$. In this case, both the system with the smaller hole and the system with the larger hole possess two minima for the vortex within the dot. With a slightly weaker field h_y, the system with $R_h = 3.0$ nm will have the outer minimum energy nearly equal to the minimum energy at the hole. With a slightly larger field h_y, the system with $R_h = 6.0$ nm will have two equivalent energy minima. In addition, the outer minima here will be fairly stable, with little chance of the vortex escaping from the dot, due to its larger diameter and deeper overall potential. It is clear even from these limited results that by adjusting the dot diameter, thickness, and hole size, bistable systems with different responses and switching fields can be designed.

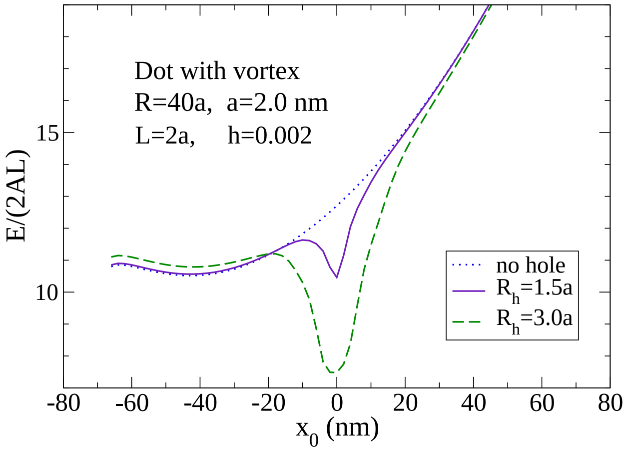

FIG. 17: (Color online) Relaxed vortex potentials for thinner dots of radius $R = 40a = 80.0$ nm, height $L = 2a = 4.0$ nm, with applied field $h_y = 0.002$, both without and with a central hole of radius R_h as indicated. Here there two minima for both systems with different hole sizes. If the field is increased, the outer minima will destabilize before the hole minima.

One further example is shown for a thinner dot, $L = 2a = 4.0$ nm, of radius $R = 40a$, in Fig. 17, for

$h_y = 0.002$. The background potential, without the hole, is shallower than that for the thicker dots. Stated differently, the local potential due to the hole is emphasized compared to the background, as already seen in Fig. 12. Even so, there are two minima present, for both hole sizes, although the outer minimum is close to being unstable. The outer minimum will destabilize around $h_y \approx 0.0024$ (see Fig. 9), reaching a field that will expel the vortex from the hole. Thus, the threshold field, which is greater than 0.0024, will simply remove the vortex entirely from the dot, without bistable switching between internal vortex states.

Still, the above results are useful because they describe the typical field strengths needed for these transitions. For the cell size $a = 2.0$ nm and Permalloy exchange length, the physical field strength relative to saturation magnetization is $H_y/M_S \approx 7h_y$. These switching events take place at very modest field strengths, which are even lower in the thinner disks.

VII. DISCUSSION AND CONCLUSIONS

A modification of the usual micromagnetics approach is developed here, constraining a desired vortex location so the the vortex-in-nanodot effective potential energy could be mapped out. For thin enough disks, the 3D demagnetization problem is replaced by a 2D problem, with special Green's functions $\vec{G}_{xy}$ and G_z to give the in-plane and out-of-plane components of the demagnetization field. An averaging procedure on G_z near the origin is used to remove its divergence. The micromagnetics is carried out on a grid with cells of size $a \times a \times L$.

The Lagrange undetermined field $\vec{\lambda}$ is included to enforce the vortex core position; it is applied over a selected core region of 24 cells in most of the calculations. Without $\vec{\lambda}$ present, the vortex would simply move to its lowest energy position. The coupling of the vortex circulation with $\vec{\lambda}$ leads to the result that a vortex displacement along one axis requires $\vec{\lambda}$ along a perpendicular axis. We can define a circulation vector of the vortex as $\vec{C} = C\hat{z}$, where $C = \pm 1$ is the sense of its rotation in the xy-plane. Then it can be seen that the force on the vortex, due to the constraint field $\vec{\lambda}$ acts in the direction of $\vec{F}_\lambda \propto \vec{C} \times \vec{\lambda}$. If the constraint is removed, we can expect that the instantaneous dynamic force on a vortex should act *oppositely* to this result. However, the coupling of the force with the vortex gyrovector leads to dynamics that involves a Magnus type interaction, hence, the vortex acceleration could be perpendicular to the directon of that force.

For small displacements x_0 from the disk center, the constraint field component λ_y is roughly proportional to the displacement, and reverses sign with the circulation. It is helpful to write this in the form $x_0 \approx -\alpha C \lambda_y$, where α is a proportionality constant that depends on the disk radius, thickness, and core area used. α can be obtained as the reciprocal of the slope near the origin of the curves in Figs. 5 and 6. Transforming λ_y into its equivalent magnetic field intensity H_λ, via relation (96), leads to a relation,

$$x_0 = -\alpha C \frac{a^2}{\lambda_{\text{ex}}^2} \frac{H_\lambda}{M_S} \tag{97}$$

The relation suggests the constraining field needed, as a fraction of the saturation field, necessary acting on the core to hold the vortex at x_0. For instance, for a disk with $R = 40a$, $L = 6a$, the inverse slope in Fig. 5 gives $\alpha \approx -650$ nm, while the ratio $a^2/\lambda_{\text{ex}}^2 \approx 1/7$. Then $x_0 \approx -(90 \text{ nm})\ (H_\lambda/M_S)$; a constraint field at 10% of saturation would secure the vortex about 9 nm from the disk center. On the other hand, to secure the vortex near $x_0 = 70$ nm requires H_λ approaching saturation. In fact, the curves in Fig. 5 turn over close to saturation, whereas, for the thinner disks of Fig. 6, values of α are larger and the core constraint field does not get close to saturation. This shows how in fact the calculational procedure is more reliable for thinner disks, as expected. The constraint field, however, is just a calculational device, and the values estimated here are not expected to have a real existence in experiments.

The effective potentials found with an applied field have minima at the unforced equilibrium vortex location. When the vortex is there, the constraint field $\vec{\lambda}$ required is zero. A relation for the vortex equilibrium location in terms of applied field holds approximately, similar to (97), but with a different proportionality constant, β:

$$x_0 = -\beta C \frac{a^2}{\lambda_{\text{ex}}^2} \frac{H_y}{M_S} \tag{98}$$

This results from a basic definition, $x_0 = -\beta C h_y$. Values of β can be estimated from the slopes near the origin in Figs. 8 and 10. For instance, again for $R = 40a$, $L = 6a$, one gets $\beta \approx 8500$ nm, whereas, for $R = 40a$, $L = 2a$, the value is much larger: $\beta \approx 24000$ nm. This quantifies the much greater ease with which the vortex position can be shifted in the thinner disks. For the thicker disks with $L = 6a$, we get $x_0 \approx -(1200 \text{ nm})\ C H_y/M_S$, and the vortex is pushed out of the disk at $H_y/M_S \approx 0.056$. For the thinner disks with $L = 2a$, the relation is $x_0 \approx -(3400 \text{ nm})\ C H_y/M_S$, and the vortex is pushed out at $H_y/M_S \approx 0.016$. Control of vortex position in these examples, then, requires very modest applied fields, that increase with disk thickness and decrease with disk radius, see Figs. 8 and 10.

Our calculations with a central nonmagnetic "hole region" confirm earlier works that show their pinning effects. In addition, the depth of the pinning potential is seen to increase quickly with the hole size. When an external magnetic field is applied, for appropriate parameters it is possible to create an effective potential with two minima for the vortex position. It should be possible to switch the vortex reversibly between these states, without expelling it entirely from the nanodot. Really, the potential in this case is two-dimensional; the dynamics during such a switching process would likely cause the vortex to move in some complex two-dimensional path between the minima.

The calculations here used only a single central hole, but can be extended to analyze systems with an off-center hole or multiple holes. For example, a pair of non-symmetrical holes will have an asymmetrical effective potential for the vortex. That arrangement could be used to to switch easily in one direction, with a more difficult switching in the opposite direction. An asymmetric metastable detection device could be designed to sense one direction of magnetic field pulses above some desired threshold, while being relatively immune to the opposite field direction. For any devices based on vortex manipulation, however, the challenge may ultimately lie in finding easy ways to discriminate the multiple states of the vortex in the dot.

---

* Electronic address: `wysin@phys.ksu.edu`; URL: `http://www.phys.ksu.edu/personal/wysin`

[1] R.P. Cowburn, J. Magn. Magn. Mater. **242-245**, 505 (2002).

[2] R.P. Cowburn, D.K. Koltsov, A.O. Adeyeye, M.E. Welland and D.M. Tricker, Phys. Rev. Lett. **83**, 1042 (1999).

[3] M. Schneider, H. Hoffmann and J. Zweck, Appl. Phys. Lett. **77**, 2909 (2000).

[4] M. Hanson, O. Kazakova, P. Blomqvist, R. Wäppling and B. Nilsson, Phys. Rev. B **66**, 144419 (2002).

[5] R. Pulwey, M. Zölfl, G. Bayreuther and D. Weiss, J. Appl. Phys. **91**, 7995 (2002).

[6] M. Hehn, K. Ounadjela, J.-P. Boucher, F. Rousseaux, D. Decanini, B. Bartenlian and C. Chappert, Science **272**, 1782 (1996).

[7] O. Kazakova, M. Hanson, P. Blomqvist and R. Wäppling, J. Appl. Phys. **90**, 2440 (2001).

[8] G. Gioia and R.D. James, Proc. R. Soc. London, Ser. A **453**, 213 (1997).

[9] J.-G. Caputo, Y. Gaididei, V.P. Kravchuk, F.G. Mertens and D.D. Sheka, Phys. Rev. B **76**, 174428 (2007).

[10] N.A. Usov and S.E. Peschany, J. Magn. Magn. Mater. **118**, L290 (1993).

[11] A. Hubert and R. Schäfer, *Magnetic Domains* (springer-Verlag, Berlin, 1998).

[12] R.L. Compton and P.A. Crowell, Phys. Rev. Lett. **97**, 137202 (2006).

[13] T. Shinjo, T. Okuno, R. Hassdorf, K. Shigeto and T. Ono, Science **289**, 930 (2000).

[14] A.R. Pereira, A.R. Moura, W.A. Moura-Melo, D.F. Carneiro, S.A. Leonel and P.Z. Coura, J. Appl. Phys. **101**, 034310 (2007).

[15] W.A. Moura-Melo, A.R. Pereira, R.L. Silva and N.M. Oliveira-Neto, J. Appl. Phys. **103**, 124306 (2008).

[16] S. Hikami and T. Tsuneto, Prog. Theor. Phys. **63**, 387 (1980).

[17] S. Takeno and S. Homma, Prog. Theor. Phys. **64**, 1193 (1980); **65**, 172 (1980).

[18] M.E. Gouvêa, G.M. Wysin, A.R. Bishop and F.G. Mertens, Phys. Rev. B **39**, 11840 (1989).

[19] G.M. Wysin, M.E Gouvêa, A.R. Bishop and F.G. Mertens, in *Computer Simulation Studies in Condensed Matter Physics*, edited by D.P. Landau, K.K. Mon and H.-B. Schüttler (Springer-Verlag, Berlin, 1988).

[20] G.M. Wysin, Phys. Rev. B **49**, 8780 (1994).

[21] C.E. Zaspel and D. Godinez, J. Magn. Magn. Mater. **162**, 91 (1996).

[22] G.M. Wysin, Phys. Lett. A **240**, 95 (1998).

[23] A.R. Pereira, Phys. Lett. A **314**, 102 (2003).

[24] A.R. Pereira, L.A.S. Mól, S.A. Leonel, P.Z. Coura, and B.V. Costa, Phys. Rev. B **68**, 132409 (2003).

[25] F.M. Paula, A.R. Pereira, L.A.S. Mól, Phys. Lett. A **329**, 155 (2004).

[26] L.A.S. Mól, A.R. Pereira, and W.A. Moura-Melo, Phys. Rev. B **67**, 132403 (2003).

[27] M. Rahm, J. Biberger, V. Umansky, and D. Weiss, J. Appl. Phys. **93**, 7429 (2003).

[28] M. Rahm, R. Höllinger, V. Umansky, and D. Weiss, J. Appl. Phys. **95**, 6708 (2004).

[29] G.M. Wysin, Phys. Rev. B **68**, 184411 (2003).

[30] A.R. Pereira, J.Magn. Magn. Mater. **279**, 396 (2004).

[31] G.M. Wysin, Phys. Rev. B **71**, 094423 (2005).

[32] C.E. Zaspel, C.M. McKennan, and S.R. Snaric, Phys. Rev. B **53**, 11317 (1996).

[33] A.R. Pereira and G.M. Wysin, Phys. Rev. B **73**, 214402 (2006).

[34] A.R. Pereira, J. Appl. Phys. **97**, 094303 (2005).

[35] A.R. Pereira, Phys. Rev. B **71**, 224404 (2005).

[36] M. Rahm, J. Stahl, W. Wegscheider, and D. Weiss, Appl. Phys. Lett. 85, 1553 (2004).

[37] T. Uhlig, M. Rahm, C. Dietrich, R. Höllinger, M. Heumann, D. Weiss and J. Zweck, Phys. Rev. Lett. **95**, 237205 (2005).

[38] Carlos J. García-Cervera, "Magnetic Domains and Magnetic Domain Walls," Ph.D. thesis, New York University (1999).

[39] Carlos J. García-Cervera, Zydrunas Gimbutas and Weinan E, J. Comp. Phys. **184**, 37 (2003).

[40] Zhongyi Huang, J. Comp. Math. **21**, 33 (2003).

[41] J. Sasaki and F. Matsubara, J. Phys. Soc. Japan **66**, 2138 (1997).

[42] Dieter Suessa, Josef Fidlera and Thomas Schrefl, Handbook of Magn. Mater. **16** 41 (2006).

[43] G.M. Wysin, Phys. Rev. B **54**, 15156 (1996).

[44] A.R. Völkel, G.M. Wysin, F.G. Mertens, A.R. Bishop and H.J. Schnitzer, Phys. Rev. B **50**, 12711 (1994) .

[45] P. Vavassori and R. Bovolenta, V. Metlushko, B. Ilic, J. Appl. Phys. **99**, 053902 (2006).

[46] G.M. Wysin, in *Electromagnetic, Magnetostatic and Exchange Interaction Vortices in Confined Magnetic Structures*, edited by Eugene Kamenetskii (Research Signpost, India 2008).

[47] K. Yu. Guslienko, V. Novosad, Y. Otani, H. Shima, and K. Fukamichi, Phys. Rev. B **65**, 024414 (2001).

[48] Q.F. Xiao, J. Rudge, B.C. Choi, Y.K. Hong and G. Donohoe, Appl. Phys. Lett. **89**, 262507 (2006).

[49] J.-G. Caputo, Y. Gaididei, F.G. Mertens and D.D. Sheka, Phys. Rev. Lett. **98**, 056604 (2007).